SAIC-01/8010:APPAT-277
June 4, 2001

NASA SUN-EARTH CONNECTIONS THEORY PROGRAM
CONTRACT NAS5-99188

The Structure and Dynamics of the Solar Corona
and Inner Heliosphere

THIRD QUARTER SECOND YEAR PROGRESS REPORT

Covering the period February 16, 2001 to May 15, 2001

Submitted by:

Zoran Mikić
Principal Investigator
Science Applications International Corporation
10260 Campus Point Drive
San Diego, CA 92121

June 4, 2001

THIRD QUARTER SECOND YEAR PROGRESS REPORT

This report covers technical progress during the third quarter of the second year of NASA Sun-Earth Connections Theory Program (SECTP) contract "The Structure and Dynamics of the Solar Corona and Inner Heliosphere," NAS5-99188, between NASA and Science Applications International Corporation, and covers the period February 16, 2001 to May 15, 2001. Under this contract SAIC and the University of California, Irvine (UCI) have conducted research into theoretical modeling of active regions, the solar corona, and the inner heliosphere, using the MHD model.

SUMMARY OF ACCOMPLISHMENTS

In this report we summarize the accomplishments made by our group during the first seven quarters of our Sun-Earth Connection Theory Program contract. The descriptions are intended to illustrate our principal results. A full account can be found in the referenced publications.

1.1. Modeling the Large-Scale Structure of the Corona and Inner Heliosphere

Our modeling of the global properties of the solar corona relies on the MHD model to describe the interaction of the solar wind with coronal magnetic fields. We initially developed a "polytropic model," in which an adiabatic energy equation with a reduced polytropic index γ is used (Parker 1963). We have used this model extensively to understand coronal observations. Illustrations of the application of this polytropic model to the "Whole Sun Month" (WSM) interval, Aug. 10–Sep. 8, 1996, are given by Linker *et al.* (1999), Breen *et al.* (1999), Gibson *et al.* (1999), and Posner *et al.* (1999).

Although the polytropic model reproduces many large-scale observations of the corona with reasonable accuracy (coronal holes, heliospheric-current-sheet crossings, coronagraph images), it fails to provide an accurate description of the solar wind. During our present program we have improved this aspect of the formulation by modeling in detail the physical mechanisms that describe the transport of energy in the corona and solar wind. One-dimensional models have demonstrated the importance of including energy transport in reproducing spacecraft solar wind measurements (Withbroe 1988; Habbal *et al.* 1995). Accordingly, we have improved the energy equation in our model to include the effects of parallel thermal conduction, radiation loss, parameterized coronal heating, and Alfvén wave acceleration. The model is described in detail by Mikić *et al.* (1999). The equations we solve are described in Appendix A.

In this improved model we use Spitzer thermal conduction along the magnetic field in the low corona, a parameterized collisionless heat flux in the outer corona (Hollweg 1978), a coronal heating source, radiation loss, and we solve the equations for the WKB evolution of Alfvén waves (Jacques 1977), so that we can include the acceleration of the solar wind by high-frequency waves. In this way we can reproduce the large-scale properties of the upper

chromosphere and transition region, as well as the emission observed from coronal loops. While there are many candidate mechanisms, there is no widely accepted theory of corona heating (e.g., Parker 1994), so we have chosen to parameterize the coronal heating function. Using this approach, we can test which coronal heating mechanisms reproduce observations (by comparing simulated X-ray and EUV emission images generated from the model with observed images, for example), as discussed in Section 1.1.2.

In our model we specify the radial magnetic field at the solar surface $r = R_s$ (e.g., from synoptic magnetic field observations, or from full-disk magnetograms); this field may evolve in time (Mikić *et al.* 1999). We can also match the transverse component of the magnetic field when such measurements become available (e.g., from the SOLIS instrument). The boundary conditions on the velocity are determined from the characteristic equations along the magnetic field. We have found that we can start the model at the top of the chromosphere, at a temperature of 20,000 K, allowing us to include the transition region in our calculation (Linker *et al.* 2001).

Using this formalism we have modeled the structure of the transition region beneath magnetic features with different topologies (i.e., open field lines in coronal holes vs. closed field lines at neutral lines). We have also self-consistently modeled the formation, support, and eruption of prominences, as described below. In the following sections we describe the application of this code to several fundamental problems of interest in coronal physics. A component of this model that can simulate the inner heliosphere has also been developed, as described in Section 1.3.1.

Even with these improvements to the energy equation, it must be recognized that a single-fluid description (inherent in the MHD model) is still a considerable approximation to the state of the corona (Habbal *et al.* 1995; Hansteen & Leer 1995; Hansteen *et al.* 1997). In particular, SOHO observations imply that the electron temperature is considerably lower in the corona than the ion temperature. One-dimensional models (e.g., Li, Esser, & Habbal 1997) have extended the theory to multiple fluids. Since it is not trivial to include these effects in multi-dimensional geometry, we will direct our attention to the single-fluid MHD model first. Eventually (not in this proposed effort) we plan to extend our formalism to include multiple fluids.

1.1.1. A Model of the Solar Wind Including the Transition Region

In order to study the relationship between coronal heating and the acceleration of the solar wind, we used our MHD code to model the solar wind flow in a 2D (axisymmetric) helmet streamer configuration (Lionello *et al.* 2001). We placed our lower radial boundary at the top of the chromosphere (at 20,000 K), as described above, to simulate the flow of the solar wind through the transition region, into the corona, and into the inner heliosphere. Figure 1 shows plasma temperature at increasingly smaller length scales, with magnetic field lines superimposed, indicating that the chromosphere extends to higher altitudes in the closed-field region above the neutral line, compared to the open-field region. The chromosphere has the

Thermal Structure of the Transition Region and Corona

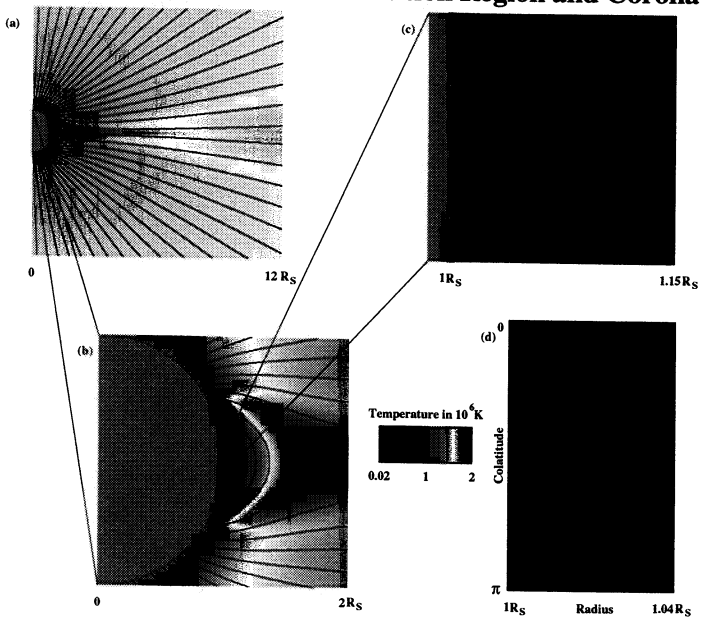

Figure 1. Plasma temperature at increasingly smaller scales with superimposed magnetic field lines for the MHD thermodynamic model (a,b,c). In panel (d), a Cartesian projection shows the structure of the transition region.

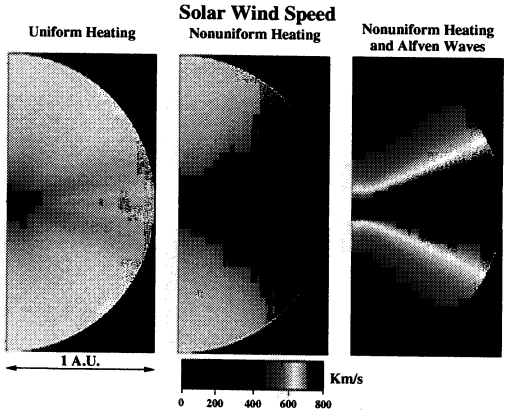

Figure 2. The solar wind speed for three different sets of parameters: uniform heating, nonuniform heating, and nonuniform heating plus Alfven wave flux. Nonuniform heating is required to obtain slow (equatorial) wind, and Alfven waves are needed to accelerate the fast wind.

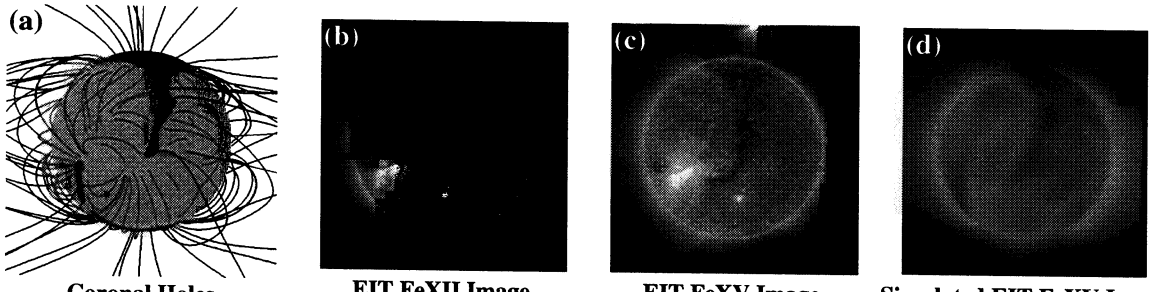

Figure 3. Comparison of EIT images of an equatorial coronal hole on August 27, 1996 with an MHD model. (a) Open field regions (black) from the MHD model. (b) EIT 195A image showing the coronal hole. (c) EIT 284A image (d) Simulated EIT 284A image using the MHD model with energy transport.

Predicting Coronal Structure During the 11 August 1999 Eclipse

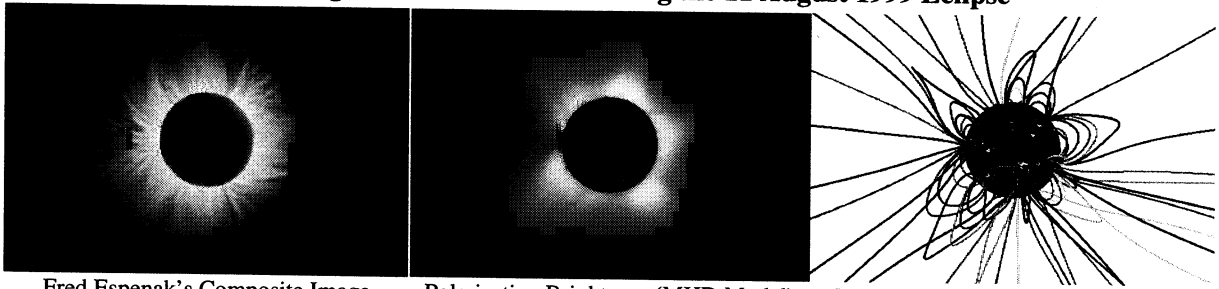

Figure 4. Comparison between a composite eclipse image created from photographs taken by Fred Espenak in Lake Hazar, Turkey with the predicted polarization brightness of the simulated solar corona from our 3D MHD model. The projected magnetic field lines from the model are also shown. Terrestrial (geocentric) north is vertically upward. The eclipse image is copyrighted 1999 by Fred Espenak.

lowest altitude near the boundary of the open/closed field region, where the conduction heating from the corona is strongest.

We have compared the results of this "chromospheric" model to those given by a model that employs a "radiative energy balance" (REB) boundary condition (as suggested by Withbroe 1988). In the REB model, the upper chromosphere and most of the transition region are not explicitly included in the calculation (i.e., the boundary temperature is set to, say, 500,000 K). The plasma density at the boundary is determined by balancing thermal conduction from the corona with radiation loss in the transition region, with a small correction for enthalpy flow. The advantage of the REB model is that it is not necessary to resolve the large gradients in the lower transition region, making for a more efficient numerical simulation of the large-scale corona. We have found that the REB model can provide a satisfactory approximation (Lionello *et al.* 2001). However, it is not well suited for investigating prominence formation, since it does not contain a chromosphere from which cold and dense material can be lifted into the corona. To study prominences we therefore use the "chromospheric" model.

After considerable experimentation, we have produced a model of the solar wind from the chromosphere to 1 AU. Figure 2 shows the radial flow speed with three different choices of parameters: uniform heating, nonuniform heating, and nonuniform heating with Alfvén wave pressure. In order to match the observed fast and slow wind velocities, mass fluxes, and temperature at 1 AU, the coronal heating scale length needs to be shorter in the streamer belt than near the poles, consistent with Withbroe (1988). We have found that an Alfvén wave flux is needed to accelerate the fast wind to values consistent with observations. Our results agree well with generic *in situ* observations of the fast and slow solar wind, as well as the observed properties in the low corona (density and temperature contrasts between the streamer belt and coronal holes).

1.1.2. EUV Emission Images

The improved energy flow description in our MHD model makes it possible to model coronal EUV emission, just as we have previously done for polarization brightness (pB). The temperature obtained from the solution can be used to predict the abundance of the coronal iron species and produce "simulated" EUV images. The 171Å, 195Å, and 284Å emission lines observed by EIT arise from the excitation of iron ions (Fe IX, Fe XII, and Fe XV). The iron population in the corona is especially sensitive to temperature and has been modeled in the CHIANTI package (Dere *et al.* 1997). The emission is dominated by collisional excitation from electron impact, and the apparent emission rate R can be written as

$$R \propto \int_{\text{los}} n_e^2 \, (e^{-\Delta E/T} / \sqrt{T}) \, F(T) \, dl \ ,$$

where the integral is taken along the line of sight. The abundance function for a particular ion species, $F(T)$, as well as the energy of the emitted photon, ΔE, depends on the line being observed.

To illustrate the idea, we show a comparison we performed for the Whole Sun Month period. In Figure 3 we compare simulated emission from our improved 3D MHD model with SOHO/EIT images for 27 August 1996. The EIT images show that an equatorial coronal hole (the "elephant's trunk") corresponds to open magnetic field lines (as predicted by the MHD model). Although there is not sufficient resolution in the calculation to reproduce the fine structure seen in EIT, the model does show low emission in the vicinity of the coronal hole. We can use a similar procedure to develop simulated Yohkoh soft X-ray images. We can also study the high-resolution emission on active-region length scales to interpret TRACE EUV emission images. This capability is essential to our proposed investigations of active regions and eruptive phenomena.

1.1.3. Comparison with Eclipse Observations

We have continued our tradition of predicting the structure of the corona prior to total solar eclipses. So far we have made four predictions using magnetic field data from the previous solar rotation. Our last prediction, of the 11 August 1999 total solar eclipse, was our most challenging yet, since this eclipse occurred close to solar maximum, when the structure of the corona was considerably more complicated than in previous cases. Our prediction was posted prior to the eclipse on the World Wide Web (`http://haven.saic.com`). Figure 4 compares our prediction with an image of the corona taken by Fred Espenak in Turkey, suggesting that our model was able to capture the complex magnetic field and streamer structure of the solar maximum Sun (Mikić *et al.* 2000). Our prediction was not as accurate as for previous eclipses, which occurred close to solar minimum. We are planning to predict the state of the corona during the forthcoming total solar eclipse in June 2001, which will be seen in Southern Africa.

1.2. The Physics of Prominences and Eruptive Phenomena

1.2.1. Photospheric Flux Changes and Solar Activity

Eruptive solar phenomena, such as coronal mass ejections, prominence eruptions, and solar flares, are believed to be initiated by the release of energy stored in the coronal magnetic field. The mechanism by which this energy is released is not well understood. Motivated by observations showing that magnetic flux emergence is associated with filament disappearances (Feynman & Martin 1995), we have found that the emergence of new magnetic flux can lead to the disruption of coronal magnetic fields and release of magnetic energy. This can occur when magnetic flux of opposite polarity emerges in the vicinity of a neutral line, canceling some of the existing flux. Recent observations have shown that magnetic flux cancellation is active at filament sites (Litvinenko & Martin 1999). Flux cancellation refers to the disappearance of magnetic fields of opposite polarity at the neutral line (Martin *et al.* 1985). We have found that flux cancellation near a neutral line, when it does not exceed a threshold value, can lead to the formation of stable magnetic flux ropes in sheared 3D arcades (Amari *et al.* 1999). When the amount of flux cancellation exceeds this threshold, the configuration erupts (Amari *et al.* 2000).

Figure 5 illustrates this process. A side view of the magnetic field lines, with the line of sight perpendicular to the neutral line, is shown. Initially, the field evolves quasi-statically; at $t = 80\tau_A$, when the instability threshold is crossed, the structure suddenly erupts upward on an ideal MHD time scale. This result is remarkably similar to a simplified analytic model of Sturrock *et al.* (2001), and the triggering mechanism is supported by observations of filament eruptions (Wang & Sheeley 1999). Our formalism for incorporating photospheric magnetic flux changes into the boundary conditions of MHD simulations is described by Mikić *et al.* (1999) and Linker *et al.* (2001).

Flux ropes have long been considered a candidate for explaining prominence support (e.g., van Ballegooijen & Martens 1989, 1990; Rust & Kumar 1994; Chen 1996; Aulanier & Demoulin 1998). A significant fraction of interplanetary CMEs are "magnetic clouds" (i.e., flux ropes, Burlaga 1988; Gosling 1990; Marubashi 1997; Bothmer & Rust 1997). The mechanism we have described is similar to that proposed by van Ballegooijen & Martens (1989); our calculations show that prominences can form in the lower corona; their eruption can disrupt helmet streamers, ejecting CMEs into the solar wind. These results are described in the following sections.

1.2.2. Prominence Formation and Eruption

Prominences (also called filaments when observed on the solar disk) support cool, dense chromospheric material (at ~ 10^4 K and 10^{10}–10^{11} cm^{-3}) against gravity in the surrounding hot, tenuous corona (~ 10^6 K and 10^7–10^9 cm^{-3}). They are observed to lie above magnetic neutral lines in the photosphere and near the base of helmet streamers. Prominences have been studied for many years, yet the means by which these structures form and are maintained are still not understood, nor is their violent eruption. Three main difficulties confront any prospective theory attempting to describe the formation and evolution of prominences: (1) Finding a magnetic configuration with "dips" (concave upward portions of flux tubes) that can gravitationally support the dense material (e.g., van Ballegooijen & Martens 1989, 1990; Antiochos *et al.* 1994; Aulanier & Demoulin 1998; Amari *et al.* 1996, 1999); (2) understanding the mechanism by which chromospheric material is trapped in the dipped field lines and held there to form a condensation (Poland & Mariska 1986; Mok *et al.* 1990; Antiochos & Klimchuk 1991; Antiochos *et al.* 1999a); and (3) elucidating the process that leads to the release of magnetic energy and the disruption of these structures (van Ballegooijen & Martens 1989; Priest & Forbes 1990; Isenberg *et al.* 1993). Item (3) is closely related to the problem of CME initiation (Forbes & Priest 1995; Linker & Mikić 1995; Low 1997; Mikić & Linker 1997; Wu & Guo 1997; Antiochos *et al.* 1999b; Lin & Forbes 2000), since these phenomena are linked observationally (Hundhausen 1997) and require the release of stored magnetic field energy and the opening of previously closed magnetic field regions (e.g., Aly 1984; Sturrock 1991; Forbes 1992; Mikić & Linker 1994; Antiochos 1998).

In the theoretical investigations referenced above, the focus was on modeling individual aspects of the problem. A complete picture of prominence formation, evolution, and eruption

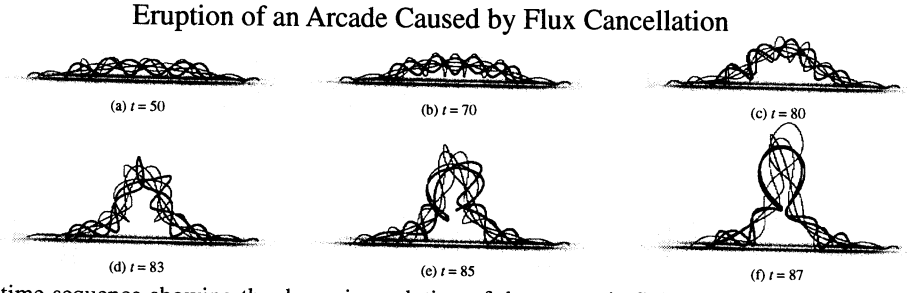

Figure 5. A time sequence showing the dynamic evolution of the magnetic field lines of a highly sheared bipole region when new flux of opposite polarity emerges from underneath the photosphere. The new flux begins to emerge at $t = 0$. At $t = 80$, an instability makes the arcade erupt violently.

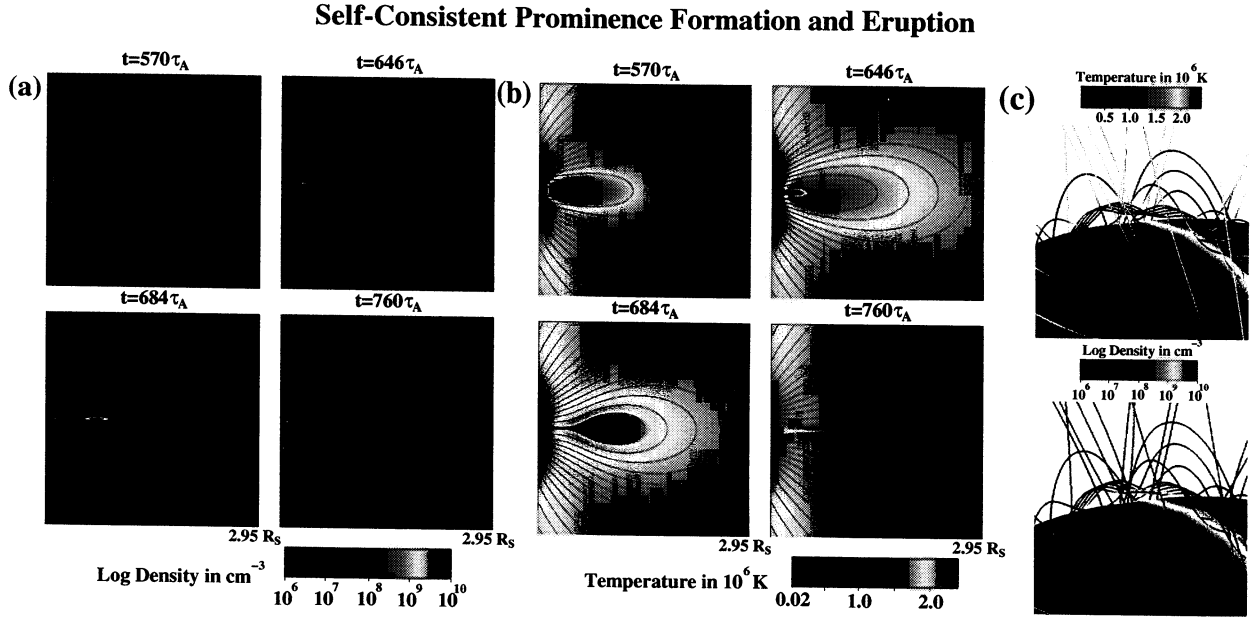

Figure 6. Evolution of the plasma density (a) and temperature (b) with superimposed magnetic field, in the self-consistent thermodynamic MHD model. Flux cancellation underneath the sheared arcade leads to the formation of a cold, dense filament-like structure. It is later ejected when the flux reduction reaches the critical threshold for eruption. In panel (c), we show magnetic field lines, colored by temperature (top) and density (bottom). The helical field supports the cold and dense prominence material against gravity.

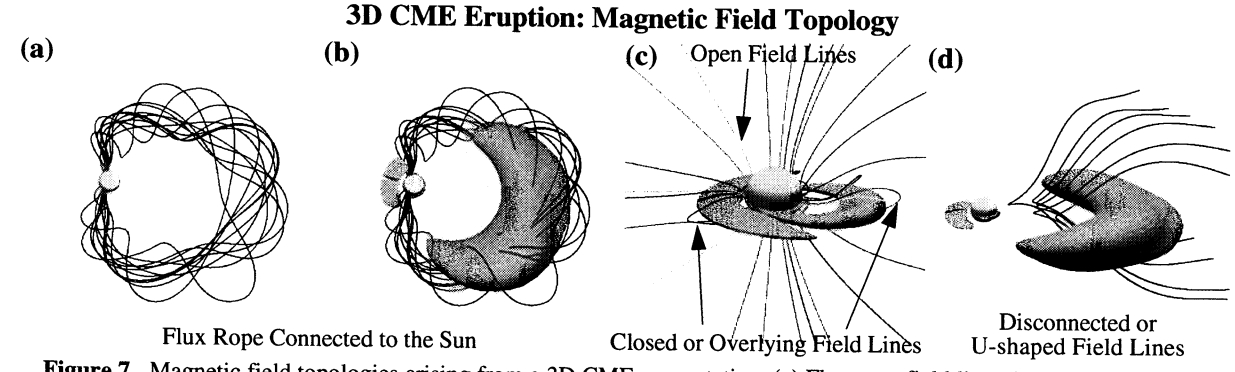

Figure 7. Magnetic field topologies arising from a 3D CME computation. (a) Flux rope field lines (viewed from above the north pole of the Sun). (b) An isosurface showing the enhanced plasma density associated with the CME. (c) Closed, unsheared field lines overlay the erupting structure; these loops are carried out into the solar wind as part of the CME. (d) Disconnected field lines are present behind the flux rope.

ultimately requires a comprehensive model of all of these processes. This is particularly true if the models are required to reproduce observations (e.g., by producing simulated emission that can be compared with SOHO or TRACE images). We have used our MHD model with energy transport to demonstrate that we can study the problem of prominence formation and eruption with a self-consistent approach. We developed a sheared helmet streamer configuration that includes the upper chromosphere and transition region (see Section 1.1.1). When flux cancellation is imposed in this model, chromospheric material is trapped on helical field lines and lifted into a stable configuration in the lower corona, as shown in Figure 6, and described in detail by Linker *et al.* (2001). Observations consistent with this picture have been reported by Lites *et al.* (1995). With further flux cancellation, the entire configuration erupts into the outer corona.

1.2.3. Interaction of Coronal Loops

High-resolution images from TRACE and SOHO show that interaction of plasma loops can lead to dynamical behavior (Pevtsov *et al.* 1996). The interaction of straight flux tubes, for instance, has been studied by Kondrasov *et al.* (1999), and the energy release was estimated by Melrose (1997). We have investigated the dynamic interaction of several two-loop configurations which are most likely to release magnetic energy rapidly, for various relative orientations between the loops (Mok *et al.* 2001). We have found that the interaction of loops with opposite magnetic helicity tends to be the most violent. The energy released is sufficient to explain a small flare (Tang *et al.* 2000).

1.2.4. Propagation of CMEs to 1 AU

In collaboration with D. Odstrcil and V. J. Pizzo of NOAA/SEC, we have studied the propagation of a simulated CME (initiated by flux cancellation) to 1 AU. The CME initiation and propagation in the inner corona was computed using our (polytropic) coronal MHD model, and the subsequent propagation through the heliosphere was carried out using the NOAA/SEC model. We have demonstrated that this approach works well (the CME passes smoothly between the adjoining boundaries of the calculation without spurious reflection or wave generation), and is significantly more efficient than a single calculation from the Sun to 1 AU. An interplanetary shock wave forms ahead of the CME, demonstrating that this is a "fast" CME. Initial results were presented at the Fall AGU 2000 meeting (Linker *et al.* 2000); additional results were presented at the Spring AGU 2001 meeting (Odstrcil *et al.* 2001; Riley *et al.* 2001a), and a manuscript is in preparation.

1.2.5. The Three-Dimensional Structure and Topology of CMEs

Using polytropic MHD computations we have investigated the 3D structure and propagation of CMEs initiated by magnetic flux cancellation. As in the 2D case, flux cancellation of sheared magnetic fields leads to the formation of a flux rope along the magnetic neutral line; in the 3D case the flux rope is anchored at both ends. Figure 7 shows magnetic field lines in the flux rope and isosurfaces of the scaled plasma density when the simulated

CME reaches the outer corona. These helical field lines remain attached to the Sun; a spacecraft intercepting this structure would not only measure field signatures similar to magnetic clouds, but would also observe a signature of bidirectional heat flux which often accompanies CMEs (Gosling *et al.* 1987). Figure 7 shows other topological features associated with the eruption, including U-shaped field lines behind the magnetic cloud, which may be associated with heat flux dropouts (McComas *et al.* 1989).

1.3. Global Modeling of the Inner Heliosphere

1.3.1. An Empirical Heliospheric Model Driven by the Coronal Magnetic Field Topology

Global models of the inner heliosphere (e.g., Pizzo 1994a,b; Riley *et al.* 1999; Riley *et al.* 2001b,c,d) can provide a necessary contextual basis with which to interpret *in situ* measurements from one or more spacecraft. Other approaches to modeling solar wind properties have been described by Usmanov *et al.* (2000) and Guhathakurta & Sittler (1999). As part of our current investigation, we have added a heliospheric component to our 3D MHD coronal model, enabling us to model the large-scale structure of the inner heliosphere out to 5 AU (Riley *et al.* 2001b,c,d). Since the time step required to advance the solution in the heliospheric component of the model is considerably larger than the time step required for the coronal solution, we separate the region of space between the solar photosphere and the Earth (or beyond) into two parts; the "coronal" region, which includes the region from the photosphere up to ~ $30R_S$, and the "heliospheric" region, which covers the region between $30R_S$ and 5 AU, where the flow is supersonic and superAlfvénic. We run the two components sequentially, with output from the coronal component providing the input into the heliospheric component. We have demonstrated that splitting the domain into two separate regions is well posed, since we were able to successfully propagate a CME from the coronal model into the heliospheric model, as described in Section 1.2.4. As discussed in detail by Riley *et al.* (2001b,c), the heliospheric model currently has an *empirical* component in the specification of the heliospheric boundary conditions. It was developed as an interim solution, so that we can immediately begin to model the structure of the solar wind in the inner heliosphere in an operational way. In our proposed program we will eliminate this empirical prescription; in the future, our heliospheric model will be driven *directly* using output from the coronal model that incorporates a more accurate energy equation.

To illustrate our results, we summarize the global structure of the heliosphere during the WSM interval in Figure 8. The heliospheric current sheet is displayed out to 5 AU, and a meridional slice of the radial velocity is shown at an arbitrary longitude. Blue corresponds to slowest speeds (~ 350 km/s) and red corresponds to fastest speeds (~ 750 km/s). Superimposed is a selection of interplanetary magnetic field lines, as well as the trajectories of the WIND and Ulysses spacecraft. The structure portrayed by Figure 8 is consistent with the general picture deduced from solar and interplanetary observations during this time period (e.g., Riley *et al.* 1999; Linker *et al.* 1999; Riley *et al.* 2001b,c). In Figure 9 we compare our MHD

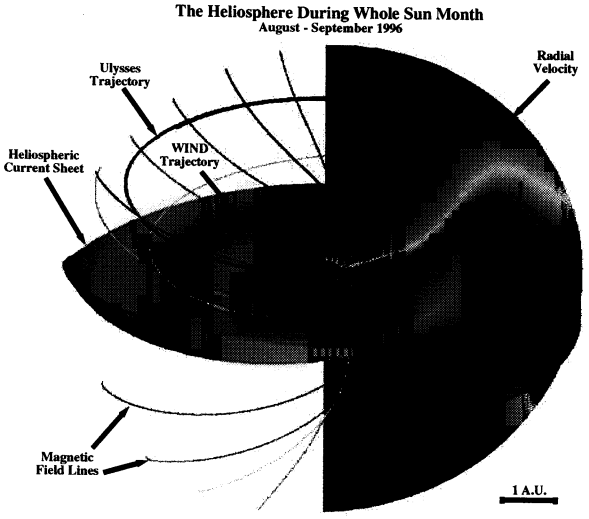

Figure 8. The large-scale structure of the solar wind speed, magnetic field lines, and heliospheric current sheet during Whole Sun Month, as deduced from a 3D MHD simulation.

Comparison of Ulysses Solar Wind Measurements with MHD Simulations

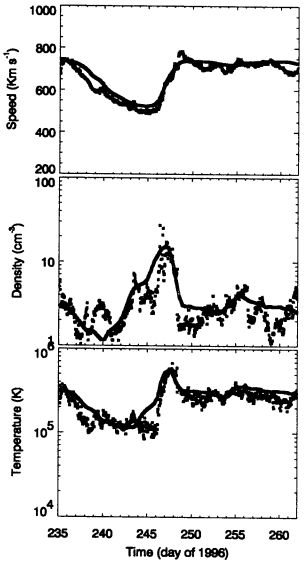

Figure 9. Comparison of Ulysses in situ measurements (blue) with 3D MHD simulation results (red) during the Whole Sun Month time interval.

Evolution of Heliospheric Structure

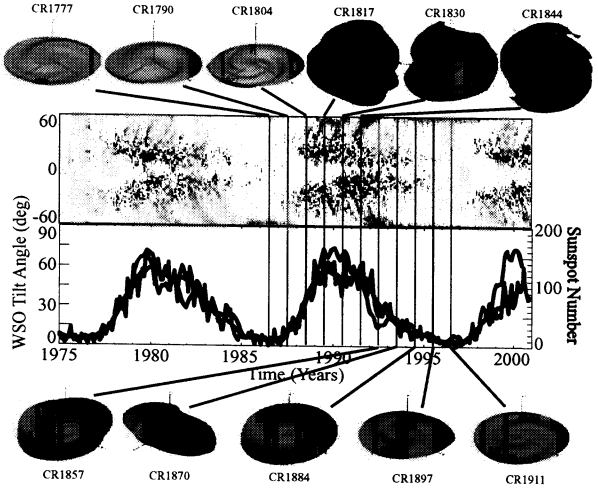

Figure 10. Evolution of several solar parameters during solar cycles 21, 22, and the ascending phase of 23, with emphasis on the evolution of the HCS during solar cycle 22. The image shows the average radial magnetic field from Kitt Peak.

Comparison of Ulysses Solar Wind Speed With MHD Simulations

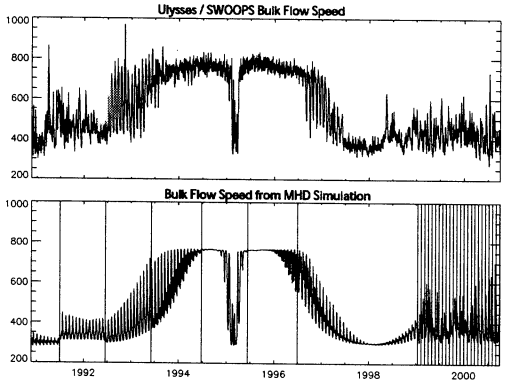

Figure 11. Comparison of Ulysses solar wind speed with the solar wind speed deduced from 3D MHD simulations. The model was run for each Carrington rotation designated by the vertical bars in the lower panel.

results directly with Ulysses *in situ* measurements, showing that the simulation successfully reproduces Ulysses' encounter of an intermediate solar wind stream.

1.3.2. Solar Cycle Dependence of the Heliosphere

We have also used this model to explore the evolution of the heliospheric current sheet (HCS) during the course of the solar cycle (Riley *et al.* 2001d). In Figure 10 we present several solar parameters, measured over a period of ~ 2-1/2 solar cycles, together with a selection of simulation results. The two central panels include data from solar cycles 21, 22, and the ascending phase of cycle 23. The lower-central panel shows the average tilt angle (black) of the HCS as derived from photospheric measurements using the WSO source-surface model, smoothed over 3 Carrington rotations, together with monthly (yearly)-averaged values of Sunspot number in red (blue). The upper-central panel is a form of the so-called "butterfly diagram" summarizing the longitudinally averaged radial component of the magnetic field, as inferred from Kitt Peak magnetograms. Blue indicates inward polarity and red indicates outward polarity.

The HCS for eleven Carrington rotations, spanning solar cycle 22 and covering mid-1986 to mid-1996, is shown above and below the central panels. Inspection of these isosurfaces reveals several noteworthy features. First, surrounding solar minimum, the HCS is better described as a flat surface with one or more folds in it, in contrast to the sinusoidal picture implied from the simple interplanetary extension of a tilted dipole. Second, folds in the HCS are typically asymmetric with respect to heliocentric distance: a fold rises more sharply on the inner radial side and falls more slowly on the outer radial side. This is a natural consequence of the dynamic interaction of the surrounding streams and is particularly effective near solar minimum. Riley *et al.* (2001d) discuss these results in more detail.

1.3.3. Understanding In Situ Solar Wind Measurements

The heliospheric model has proved to be helpful in interpreting *in situ* solar wind measurements from WIND, ACE, and Ulysses during a number of phases of the solar cycle (Riley *et al.* 2001b,c,d), reproducing many of the large-scale features of the observations. We have also used the near-solar-maximum results to speculate on the structure of the high-latitude solar wind that Ulysses would encounter during its traversal of the southern and northern solar poles in 2000 and 2001, respectively (Riley *et al.* 2001c). Our results suggested that, due to the presence of equatorial coronal holes, the ordered pattern of CIR tilts and their associated shocks, which was observed during Ulysses' initial southward excursion in 1992, would likely disappear completely as Ulysses moves toward the South Pole. We also suggested that Ulysses would encounter fast streams but would not remain within them for more than a fraction of a solar rotation, and that crossings of the HCS would persist up to at least ~ 70° heliographic latitude. The most recent measurements from Ulysses (April 2001) are in general agreement with these results.

In Figure 11 we compare Ulysses/SWOOPS wind speed measurements with our simulation results, obtained by "flying" the Ulysses trajectory through a sequence of

simulations. The solid vertical lines in the lower panel mark the Carrington rotations for which we ran simulations. Thus prior to 1999, the comparison is of limited value, since approximately 1 year is represented by a single Carrington rotation. Nevertheless, this comparison serves to illustrate how simulation data can be used to provide a global context for *in situ* solar wind observations. It is apparent that the MHD model reproduces the large-scale changes associated with transitions between fast and slow solar wind streams encountered by Ulysses.

REFERENCES

Aly, J. J. 1984, *Ap. J.*, **283**, 349.

Amari, T., Luciani, J. F., Aly, J. J., and Tagger, M. 1996, *Ap. J.*, **306**, 913.

Amari, T., Luciani, J. F., Mikić, Z., and Linker, J. A. 1999, *Ap. J., Lett*, **518**, L57.

Amari, T., Luciani, J. F., Mikić, Z., and Linker, J. A. 2000, *Ap. J., Lett*, **529**, L49.

Antiochos, S. K. 1998, *Ap. J. Lett.*, **502**, L181.

Antiochos, S. K., Dahlburg, R. B., and Klimchuk, J. A. 1994, *Ap. J., Lett*, **420**, L41.

Antiochos, S. K., DeVore, C. R., and Klimchuk, J. A. 1999b, *Ap. J.*, **510**, 485.

Antiochos, S. K., and Klimchuk, J. A. 1991, *Ap. J.*, **378**, 372.

Antiochos, S. K., MacNeice, P. J., Spicer, D. S., and Klimchuk, J. A. 1999a, *Ap. J.*, **512**, 985.

Aulanier, G. and Demoulin, P. 1998, *Ap. J.*, **329**, 1125.

Bothmer, V., and Rust, D. M. 1997, (N. Crooker, J. Joselyn and J. Feynman, eds.), in *Coronal Mass Ejections, Geophysical Monograph,* **99**, American Geophysical Union, p.139.

Breen, Mikić, Z., Linker, J. A., Lazarus, A. J., Thompson, B. J., Biesecker, D. A., Moran, P. J., Varley, C. A., Williams, P. J. S., and Lecinski, A., 1999, *J. Geophys. Res.*, **104**, 9847.

Burlaga, L. F. 1988, *J. Geophys. Res.*, **93**, 7217.

Chen, J. 1996, *J. Geophys. Res.*, **101**, 27499.

Dere, K. P., Landi, E., Mason, H. E., Monsignori Fossi, B.C., and Young, P. R. 1997, *Astron. Astrophys. Suppl. Ser.*, **125**, 149.

Feynman, J., and Martin, S. F. 1995, *J. Geophys. Res.*, **100**, 3355.

Forbes, T. G. 1992, "Proceedings of IAU Colloquium #133," (Z. Svestka, B. V. Jackson, and M. E. Machado, eds.) Springer-Verlag, New York.

Forbes, T. G., and Priest, E. R. 1995, *Ap. J.*, **446**, 377.

Gibson, S. E., Biesecker, D., Guhathakurta, M., Hoeksema, J. T., Lazarus, A. J., Linker, J. A., Mikić, Z., Pisanko, Y., Riley, P., Steinberg, J., Strachan, L., Szabo, A., and Thompson, B. J. 1999, *Ap. J.*, **520**, 871.

Gosling, J. T. 1990, in Physics of Magnetic Flux Ropes (C. T. Russel, E. R. Priest, and L. C. Lee, eds.), *Geophysical Monograph* **58**, American Geophysical Union, p. 330.

Gosling, J. T., Baker, D. N., Bame, S. J., Feldman, W. C., Zwickl, R. D., and Smith, E. J. 1987, *J. Geophys. Res.*, **92**, 8519.

Guhathakurta, M., and Sittler, E., in *Solar Wind Nine* 1999, (S. R. Habbal, R. Esser, J. V. Hollweg, and P. A. Isenberg eds), *AIP Conference Proceedings,* API, Woodbury, New York, ***385***, pp. 79-82.

Habbal, S. R., Esser, R., Guhathakurta, M., and Fisher, R. R. 1995, *J.* Geophys. Res. Lett., **22**, 1465.

Hansteen, V. H., and Leer, E. 1995, *J. Geophys. Res* , **100**, 21577.

Hansteen, V. H., Leer, E., and Holzer, T. E. 1997, *Ap. J.*, **482**, 498.

Hollweg, J. V. 1978, *Reviews of Geophysics*, **16**, 689.

Hundhausen, A. J. 1997, *in Coronal Mass Ejections,* (N. Crooker, J. Joselyn, and J. Feynman, eds.), *Geophysical Monograph,* **99**, American Geophysical Union, p. 1.

Isenberg, P. A., Forbes, T. G., and Demoulin, P. 1993, *Ap. J.*, **417**, 368.

Jacques, S. A. 1977, *Ap. J.*, **215**, 942.

Jiao, L. McClymont, A. N., and Mikić, Z. 1997, *Solar Phys.*, **174**, 311.

Kondrashov, D., Feynman, J., Liewer, P.C. and Ruzmaikin, A. 1999, *Ap. J.*, **519**, 884.

Li, X., Esser, R., & Habbal, S. R. 1997, *J. Geophys. Res.*, **102**, 17419.

Lin, J., and Forbes, T. G. 2000, *J. Geophys. Res.,* **105**, 2375.

Linker, J. A., Lionello, R., Mikić, Z., and Amari T. 2001, to appear in *J. Geophys. Res.*

Linker, J. A., and Mikić, Z. 1995, *Ap. J., Lett,* **438,** L45.

Linker, J. A., and Mikić, Z. 1997, *in Coronal Mass Ejections*, (N. Crooker, J. Joselyn and J. Feynman, eds.), *Geophysical Monograph,* **99**, American Geophysical Union, p. 269.

Linker, J. A., Mikić, Z., Biesecker, D. A., Forsyth, R. J., Gibson, S. E., Lazarus, A. J., Riley, P., Szabo, A., and Thompson, B. J. 1999, *J. Geophys. Res.* **104**, 9809.

Linker, J. A., Mikić, Z., Lionello, R., Riley, P., Odstrcil, D., Pizzo, V. J., and Goodrich, C. C., 2000, *EOS Trans.,* American Geophysical Union, **81**, F975, Fall AGU meeting.

Lionello, R., Linker, J. A., and Mikić, Z. 2001, *Ap. J* **546,** 542.

Lites, B. W., Low, B. C., Martinez V., Pillet, Segraves, P., Skumanich, A., Frank, Z. A., Shine, R. A., and Tsuneta, S. 1995, *Ap. J.*, **446**, 877.

Litvinenko, Y. E., and Martin, S. R. 1999, *Solar Phys.*, **190**, 45.

Low, B. C. 1997, *in Coronal Mass Ejections,* (N. Crooker, J. Joselyn and J. Feynman, eds.), *Geophysical Monograph,* **99**, American Geophysical Union, p. 39.

Martin, S. F., Livi, S. H. B., and Wang, J. 1985, *Australian J. Phys.* **38**, 929.

Marubashi, K. 1997, *in Coronal Mass Ejections* (N. Crooker, J. Joselyn and J. Feynman, eds.), *Geophysical Monograph,* **99**, American Geophysical Union, p 147.

McClymont, A. N., Jiao, L., and Mikić, Z. 1997, *Solar Phys.*, **174**, 191.

McComas, D. J., Gosling, J. T., Phillips, J. L., Bame, S. J., Luhmann, J. G., and Smith, E. J. 1989, *J. Geophys. Res.,* **94**, 6907.

Melrose, D.B. 1997, *Ap. J.*, **486**, 521.

Mikić, Z., and Linker, J. A. 1994, *Ap. J.*, **430**, 898.

Mikić, Z., and Linker, J. A. 1996, in *Solar wind 8,* (D. Winterhalter, J. T. Gosling, S. R. Habbal, W. S. Kurth, and M. Neugebauer, eds), *AIP Conference Proceedings,* API, Woodbury, New York, **382**, p. 104.

Mikić, Z., and Linker, J. A. 1997, *in Coronal Mass Ejections* (N. Crooker, J. Joselyn, and J. Feynman, eds.), *Geophysical Monograph,* **99**, American Geophysical Union, p. 57.

Mikić, Z., Linker, J. A., and Schnack, D. D. 1996, *in Solar Drivers of Interplanetary and Terrestrial Disturbances* (K. S. Balasubramaniam, S. L. Keil, and R. N Smartt, eds.), *Astron. Soc. Pac. Conf.*, **95**, p. 108.

Mikić, Z., Linker, J. A., Schnack, D. D., Lionello, R., and Tarditi, A. 1999, *Phys. Plasmas*, **6**, 2217.

Mikić, Z., Linker, J. A., Riley, P., and Lionello, R. 2000, *in "The Last Total Solar Eclipse of the Millennium,"* (W. Livingston and A. Özgüc, eds.), *Astronomical Society of the Pacific Conference Series*, **205**, 162.

Mikić, Z., and McClymont, A. N. 1994, in *Solar Active Region Evolution: Comparing Models with Observations* (K. S. Balasubramaniam and G. W. Simon, eds), Astron. Soc. Pac., Conf. Series, **68**, 225.

Mok, Y., Drake, J. F., Schnack, D. D., and Van Hoven, G. 1990, *Ap. J.*, **359**, 228.

Mok, Y., Mikić, Z., and Linker, J. A. 2001, *Ap. J.*, in press.

Odstrcil, D., Pizzo, V. J., Linker, J. A., Lionello, R., Mikić, Z., and Luhmann, J. G. 2001, *EOS Trans. AGU*, **81**, Spring AGU meeting.

Parker, E. N. 1963, *Ap. J.*, **138**, 552.

Parker, E. N. 1994, *Spontaneous Current Sheets in Magnetic Fields* (New York: Oxford).

Pevtsov, A.A., Canfield, R.C. and Zirin, H. 1996, *Ap. J.*, **473**, 533.

Pizzo, V. J. 1994a, *J. Geophys. Res.*, **99**, 4173.

Pizzo, V. J. 1994b, *J. Geophys. Res.*, **99**, 4185.

Poland, A. I., and Mariska, J. T. 1986, *Solar Phys.*, **104**, 303.

Posner, A. et al., 1999, *J. Geophys. Res., 104,* 9881.

Priest, E. R., and Forbes, T. G. 1990, *Solar Phys.*, **126**, 319.

Riley, P., Gosling, J. T., McComas, D. J., Pizzo, V. J., Luhmann, J. G., Biesecker, D., Forsyth, R. J., Hoeksema, J. T., Lecinski, A., and Thompson, B. J. 1999, Relationship between Ulysses plasma observations and solar observations during the Whole Sun Month campaign, *J. Geophys. Res.*, **104**, 9871.

Riley, P, Linker, J. A., Lionello, R., Mikić, Z., Odstrcil, D., Pizzo, V. J., Zurbuchen, T. H., and Lario, D. D. 2001a, *EOS Trans. AGU*, **81**, Spring AGU meeting.

Riley, P., Linker, J. A., and Mikić, Z. 2001c, *J. Geophys. Res.*, in press.

Riley, P., Linker, J. A. and Mikić, Z. 2001d, submitted to *J. Geophys. Res.*

Riley, P., Linker, J. A., Mikić, Z., and Lionello, R. MHD Modeling of the Solar Corona and Inner Heliosphere: Comparison with Observations, accepted for publication in the *Chapman Conference on Space Weather*, to be published by the American Geophysical Union, Washington D.C., 2001b.

Rosner, R., Tucker, W. H., and Vaiana, G. S. 1978, *Ap. J.*, **220**, 643.

Rust, D. M., and Kumar, A. 1994, *Solar Phys.*, **155**, 69.

Sturrock, P. A. 1991, *Ap. J.*, **380**, 655.

Sturrock, P.A., Weber, M., Wheatland, M.S. and Wolfson, R. 2001, *Ap. J.*, **548**, 492.

Tang, Y.H., Li, Y.N., Fang, C., Aulanier, G., Schmieder, B., Demoulin, P. and Sakurai, T. 2000, *Ap. J.*, **534**, 482.

Usmanov, A. V., Goldstein, M. L., Besser, B. P. and Fritzer, J. M. 2000, *J. Geophys. Res.*, **105**, 12,675.

van Ballegooijen, A. A., and Martens, P. C. H. 1989, *Ap. J.*, **343**, 971.

van Ballegooijen, A. A., and Martens, P. C. H. 1990, *Ap. J.*, **361**, 283.

Wang, Y.M. and Sheeley, N.R. 1999, *Ap. J., Lett.* **510**, 157.

Withbroe, G. L. 1988, *Ap. J.*, **325**, 442.

Wu, S. T., and Guo, W. P. 1997, *in Coronal Mass Ejections* (N. Crooker, J. Joselyn, and J. Feynman, eds.), *Geophysical Monograph,* **99**, American Geophysical Union, p. 83.

APPENDIX A

MHD EQUATIONS USED IN THE GLOBAL CORONAL MODEL

MHD EQUATIONS

For MHD computations to be accurate enough to compare with detailed emission images and predict solar wind properties at 1 AU, significant extensions to the usual MHD equations are necessary. Following earlier one-dimensional models (Withbroe 1988; Habbal *et al.* 1995), the energy equation in our model to include the effects of parallel thermal conduction, radiation loss, parameterized coronal heating, and Alfvén wave acceleration, and solves the following MHD equations:

$$\nabla \times \mathbf{B} = \frac{4\pi}{c}\mathbf{J} \ , \tag{A1}$$

$$\nabla \times \mathbf{E} = -\frac{1}{c}\frac{\partial \mathbf{B}}{\partial t} \ , \tag{A2}$$

$$\mathbf{E} + \frac{1}{c}\mathbf{v} \times \mathbf{B} = \eta \mathbf{J} \ , \tag{A3}$$

$$\frac{\partial \rho}{\partial t} + \nabla \cdot (\rho \mathbf{v}) = 0 \ , \tag{A4}$$

$$\rho\left(\frac{\partial \mathbf{v}}{\partial t} + \mathbf{v} \cdot \nabla \mathbf{v}\right) = \frac{1}{c}\mathbf{J} \times \mathbf{B} - \nabla p - \nabla p_w + \rho \mathbf{g} + \nabla \cdot (\nu \rho \nabla \mathbf{v}) \ , \tag{A5}$$

$$\frac{\partial p}{\partial t} + \nabla \cdot (p\mathbf{v}) = (\gamma - 1)\left(-p \nabla \cdot \mathbf{v} + S\right) \ , \tag{A6}$$

$$S = -\nabla \cdot \mathbf{q} - n_e n_p Q(T) + H_{\rm ch} + H_{\rm d} + D \ , \tag{A7}$$

where $\mathbf{B}$ is the magnetic field, $\mathbf{J}$ is the current density, $\mathbf{E}$ is the electric field, ρ, $\mathbf{v}$, p, and T are the plasma mass density, velocity, pressure, and temperature, and the wave pressure p_w represents the acceleration due to Alfvén waves. The gravitational acceleration is $\mathbf{g}$, $\gamma = 5/3$ is the ratio of specific heats, η is the resistivity, ν is the viscosity, $H_{\rm ch}$ is the coronal heating source, D is the Alfvén wave dissipation term, n_e and n_p are the electron and proton density, and $Q(T)$ is the radiation loss function (Rosner *et al.* 1978). The term $H_{\rm d} = \eta J^2 + \nu \nabla \mathbf{v} : \nabla \mathbf{v}$ represents heating due to viscous and resistive dissipation. In the collisional regime (below ~ $10R_s$), the heat flux is $\mathbf{q} = -\kappa_{\|} \hat{\mathbf{b}} \hat{\mathbf{b}} \cdot \nabla T$, where $\hat{\mathbf{b}}$ is the unit vector along $\mathbf{B}$, and $\kappa_{\|} = 9 \times 10^{-7}\ T^{5/2}$ is the Spitzer value of the parallel thermal conductivity. In the collisionless regime (beyond ~ $10R_s$), the heat flux is given by $\mathbf{q} = \alpha n_e k T \mathbf{v}$, where α is a parameter (Hollweg 1978). Since it is presently not known in detail what heats the solar corona, the coronal heating source $H_{\rm ch}$ is a parameterized function. A simple form is

$$H_{\rm ch} = H_{\rm o}(\theta) \exp\left[-(r - R_s)/\lambda(\theta)\right] \ , \tag{A8}$$

where $H_{\rm o}(\theta)$ expresses the latitudinal variation of the volumetric heating, and $\lambda(\theta)$ expresses the latitudinal variation of the heating function scale length. [In practice, this function can be tailored to match the scaling of different coronal heating models). Note that the simplified polytropic model is obtained by setting $S = 0$ in Eq. (A6), $p_w = 0$ in Eq. (A5), and $\gamma = 1.05$.

Since the acceleration of the solar wind by Alfvén waves occurs on a spatial and time scale that is below the spatial and time resolution of our global numerical model, the wave pressure p_w is evolved using an equation for the time-space averaged Alfvén wave energy density ε (Jacques 1977),

$$\frac{\partial \varepsilon}{\partial t} + \nabla \cdot \mathbf{F} = \mathbf{v} \cdot \nabla p_w - D \ , \qquad \text{(A9)}$$

where $\mathbf{F} = (\frac{3}{2}\,\mathbf{v} + \mathbf{v}_A)\varepsilon$ is the Alfvén wave energy flux, $v_A = B/\sqrt{4\pi\rho}$ is the Alfvén speed, and $p_w = \frac{1}{2}\varepsilon$. The Alfvén wave velocity is $\mathbf{v}_A = \pm\hat{\mathbf{b}}v_A$; in a multi-dimensional implementation, it is necessary to transport two Alfvén wave fields (waves parallel and antiparallel to **B**), which are combined to give ε. The Alfvén wave energy density ε is related to the space-time average of the fluctuating component of the magnetic field δB by $\varepsilon = <\delta B^2>/4\pi$. The dissipation term D expresses the nonlinear dissipation of Alfvén waves in interplanetary space and is modeled phenomenologically (Hollweg 1978).

We have developed three-dimensional codes to solve MHD equations (A1)–(A9) in spherical coordinates (r,θ,ϕ) and equations (A1)-(A7) (without Alfvén wave acceleration) in Cartesian coordinates. The spherical code have been used extensively to model CMEs (Mikić & Linker 1994, 1997; Linker & Mikić 1995, 1997; Linker *et al.* 2001), coronal structure (Mikić & Linker 1996; Linker *et al.* 1999; Mikić *et al.* 1999, 2000; Lionello *et al.* 2001), and heliospheric structure (Riley *et al.* 2001b,c). The Cartesian code uses a very similar algorithm and has been used to study active regions (Mikić & McClymont 1994; Mikić *et al.* 1996; Jiao *et al.* 1997; McClymont *et al.* 1997; Mok *et al.* 2001).